Journal of the Mechanics and Physics of Solids 111 (2018) 358–374

Contents lists available at ScienceDirect

Journal of the Mechanics and Physics of Solids

journal homepage: www.elsevier.com/locate/jmps

Experimental validation of plastic constitutive hardening relationship based upon the direction of the Net Burgers Density Vector

Abdulhamit Sarac*, Jeffrey W. Kysar

Department of Mechanical Engineering, Columbia University, New York, NY 10027, New York

ARTICLE INFO

Article history:
Received 3 March 2017
Revised 12 October 2017
Accepted 12 November 2017
Available online 14 November 2017

Keywords:
Single crystal plasticity
Finite Element Simulations
β-fields
Lattice rotation
Slip systems

ABSTRACT

We present a new methodology for experimental validation of single crystal plasticity constitutive relationships based upon spatially resolved measurements of the direction of the Net Burgers Density Vector, which we refer to as the β-field. The β-variable contains information about the active slip systems as well as the ratios of the Geometrically Necessary Dislocation (GND) densities on the active slip systems. We demonstrate the methodology by comparing single crystal plasticity finite element simulations of plane strain wedge indentations into face-centered cubic nickel to detailed experimental measurements of the β-field. We employ the classical Peirce–Asaro–Needleman (PAN) hardening model in this study due to the straightforward physical interpretation of its constitutive parameters that include latent hardening ratio, initial hardening modulus and the saturation stress. The saturation stress and the initial hardening modulus have relatively large influence on the β-variable compared to the latent hardening ratio. A change in the initial hardening modulus leads to a shift in the boundaries of plastic slip sectors with the plastically deforming region. As the saturation strength varies, both the magnitude of the β-variable and the boundaries of the plastic slip sectors change. We thus demonstrate that the β-variable is sensitive to changes in the constitutive parameters making the variable suitable for validation purposes. We identify a set of constitutive parameters that are consistent with the β-field obtained from the experiment.

1. Introduction

The central focus of this paper is to introduce a new methodology for the experimental validation of plastic constitutive relationships based upon measurements of a quantity denoted herein as β that characterizes the *direction of the Net Burgers Density Vector* associated with the presence of Geometrically Necessary Dislocation (GND) densities. The direction of the Net Burgers Density Vector identifies the active plastic slip systems that have contributed to the GND density as well as the relative contributions of the active slip systems (Kysar et al., 2010; Sarac et al., 2016). The principal advantage of the validation methodology is that the Net Burgers Density Vector characterizes both the *material state* as well as the *deformation state* by determination of the *active slip systems*, whereas other variables used for experimental validation characterize only the

* Corresponding author.
E-mail address: as3525@columbia.edu (A. Sarac).

https://doi.org/10.1016/j.jmps.2017.11.010
0022-5096/

deformation state. Hence in principle the methodology can be used to validate directly the evolution of the state variables that enter into the constitutive relationship.

Plasticity constitutive relationships predict the current strength of the plastic slip systems based upon the underlying crystal structure as well as the history of prior plastic deformation. A constitutive relationship can be represented succinctly by the evolution of the plastic yield surface with plastic deformation. Traditional experimental validation methods are based upon determining the shape and evolution of the yield surface in single crystal and polycrystalline materials include: tension, compression, bending, torsion and simultaneous combinations of those loadings, thin film bulge test, bending and indentation, among others (e.g. Uchic et al., 2004; Lee et al., 2007a; Wei et al., 2007; Lee et al., 2008; 2007b; Yilmaz and Kysar, 2013; Ghazi and Kysar, 2016).

For single crystal plasticity, the yield surface is a polygon in stress-space and active slip systems are determined based upon whether the applied stress state coincides with a facet (leading to slip on a single slip system) or a vertex (leading to simultaneous slip on multiple slip systems) of the yield surface. As deformation proceeds, slip system hardening and lattice rotation lead to distortion and rotation of the yield surface. The most direct method to probe experimentally the yield surface and its evolution is to deform a single crystal under single slip conditions and subsequently excise a new specimen from the first and load it in an orientation that induces plastic slip on a previously latent slip system (e.g. Wu et al., 1991, and references therein).

These traditional experimental methods measure the average response of a specimen material via work conjugate pairs of force and displacement quantities at the specimen boundaries. Such methods are often augmented with spatially-resolved measurements of the inhomogeneous deformation state. Traditionally this has been accomplished via moiré or interferometric methods (e.g. Shield and Kim, 1994; Bastawros and Kim, 2000), but more recently Digital Image Correlation (DIC) method has proven effective (e.g. Sutton et al., 1986; Bruck et al., 1989; Vendroux and Knauss, 1998; Lu and Cary, 2000; Hung and Voloshin, 2003; Pan et al., 2009; Wu et al., 2016). In combination, these methods can be used to probe the form of deformation fields associated with boundary value problems that predict deformation fields with distinguishing features such as those associated with crack tips, voids and indentations.

Deformation measurements provide indirect information about material behavior but they do not probe directly the state of the material in the sense that they do not quantify state variables that enter into plasticity constitutive relationships. For example, plasticity constitutive relationships dating back to Taylor (1934) employ the accumulated dislocation content on individual slip systems as a state variable. More recently, the Geometrically Necessary Dislocation (GND) density or the related Nye dislocation density tensor (Nye, 1953) components have been employed as state variables in constitutive relationships for strain gradient plasticity constitutive relationships (e.g. Gurtin et al., 2007; Kuroda and Tvergaard, 2008; Öztop et al., 2013). Deformation measurements alone are unable to measure these state variables.

The new experimental validation methodology for crystal plasticity constitutive relationships is based upon measurements of the Nye dislocation density tensor from which the Net Burgers Density Vector as well as GND densities on individual slip systems can be calculated. The direction of the Net Burgers Density Vector, β, is the quantity of interest for this new validation method. Single crystal plasticity predictions of the spatial distribution of β, that we refer to a β-field, are compared to experimental measurements of the β-field. The specific boundary value problem we consider herein is plane strain wedge indentation into a single face-centered cubic crystal. Our results demonstrate that the spatial variation of β is sensitive to hardening parameters that enter into plastic constitutive relationships and thus can be used as a means for their experimental validation.

The present paper draws on several disparate bodies of work so it has a lengthy background discussion in Section 2 that is intended to be largely self-contained. Specifically we first motivate use of the Net Burgers Density Vector direction, β, as a validation variable by showing that the domain of a single crystal plasticity boundary value problem typically can be decomposed into *plastic slip sectors* within which a well-defined subset of plastic slip systems is active. We then discuss plane strain wedge indentation into a single crystal and describe analytical and computational predictions of how active slip systems vary with position. We also discuss briefly the experimental methods used to measure the Nye dislocation density tensor. In Section 4, we discuss detailed Finite Element Method (FEM) calculations of the experiments. This includes a description of the plasticity constitutive hardening relationship and its respective parameters employed in the Peirce–Asaro–Needleman (PAN). We purposely choose to employ the classical PAN constitutive model because of the straightforward physical interpretation of its material parameters. The effects of the constitutive parameters on numerical predictions of the β-fields are compared to experimental measurements in Section 5. Variations of the plastic slip and slip rate on individual slip systems for the PAN constitutive model are presented. Furthermore, the spatial distributions of stress are plotted in stress space as a means to identify plastic slip sectors and their boundaries. Discussion and concluding remarks are given in Section 6. To make the present paper more condensed and readable, additional information and figures are moved from the main text to On-line Supplementary Information (Section A).

2. Background

We first motivate use of the Net Burgers Density Vector direction, β, as a validation variable. Plastic deformation is typically governed by a hyperbolic partial differential equation (PDE) exemplified by slip line theory in the limit of infinitesimal deformations and rigid, ideally plastic constitutive behavior (e.g. Booker and Davis, 1972; Rice, 1973; Kysar et al., 2005). A hyperbolic PDE can be solved via the Method of Characteristics by expressing the PDE in a coordinate frame that reduces

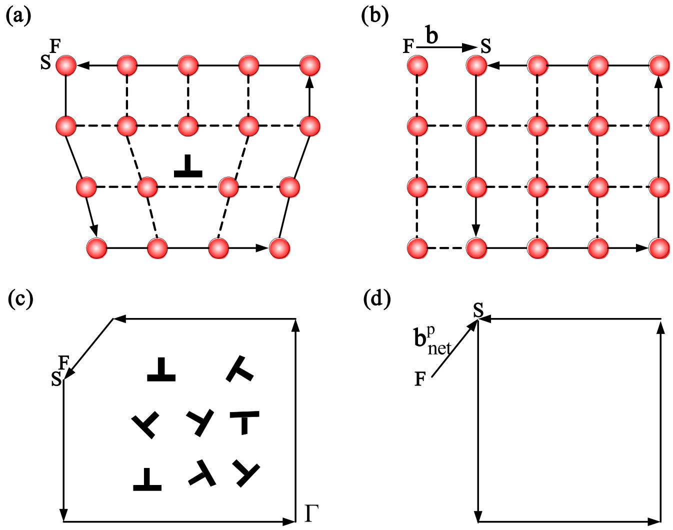

Fig. 1. Crystal lattice and the Burgers circuits: (a) Crystal lattice with a single dislocation, (b) the Burgers vector, **b**, (c) Crystal body with multiple dislocations (d) the net Burgers vector, $\mathbf{b}^p_{net}$ (Sarac et al., 2016).

it to an ordinary differential equation (ODE). The new coordinate axes are referred to as *characteristics* that are, in general, curvilinear. In the context of plasticity the characteristics correspond physically to directions of plastic slip; for single crystal plasticity the characteristics coincide with the dislocation slip direction denoted here by the unit vector **s**, as well as the dislocation slip plane normal denoted by the unit vector **n** (e.g Rice, 1973; Kysar et al., 2005).

Discontinuities are commonly observed in solutions to hyperbolic PDEs. When applied to plastic deformation such discontinuities are usually in terms of stress and velocity. In addition, solutions of single crystal plasticity boundary value problems exhibit discontinuities in active slip systems as a consequence of the polygonal yield surface. The plastically deforming domain is divided into subdomains within which well-defined subsets of complete set of slip systems are active. We refer to such regions as *plastic slip sectors*. The boundaries between the plastic slip sectors represent spatial discontinuities in active slip systems. Plastic slip sectors in single crystals manifest themselves in deformation fields associated with crack tips (Kysar, 2000; 2001a; 2001b; Rice, 1987), cylindrical voids (Gan and Kysar, 2007; Gan et al., 2006; Kysar et al., 2005), flat punches (Rice, 1973), a Gaussian pressure distribution (Wang et al., 2008), and angled indenters (Saito and Kysar, 2011).

The Burgers vector, **b**, is a fundamental quantity in crystal plasticity that denotes the direction and magnitude of slip across adjacent atomic planes due to the passage of a single dislocation. The Burgers vector is evaluated by taking a circuit (denoted herein as Γ) on an atomic plane starting at an initial point **S** and ending at a terminal point **F** that is coincident with **S** in a defect-free lattice. Upon the introduction of a single dislocation line that pierces the plane of Γ, the circuit no longer closes. The Burgers vector (or closure failure vector) is defined as the vector necessary to close the circuit as depicted in Fig. 1(a) and (b). When multiple dislocations pierce Γ the closure failure vector between **S** and **F** represents the signed vector sum of the individual Burgers vectors as illustrated in Fig. 1(c) and (d). This vector is referred to as the *Net Burgers Vector* denoted as $\mathbf{b}^p_{net}$. Normalization of the net Burgers vector by the scalar area, A, encompassed by Γ defines the *Net Burgers Density Vector*, which is expressed as $\mathbf{B} = \mathbf{b}^p_{net}/A$; it is also commonly called the *net closure failure density vector*. This normalization process renders the concept of net Burgers vector a continuum quantity. The magnitude of **B** is closely related to the concept of Geometrically Necessary Dislocation (GND) density. The direction of **B** provides insight into the individual slip systems that contribute to the total GND density as well as the apportionment of those slip systems within the total GND density (Kysar et al., 2010; Sarac et al., 2016). In recently published experiments, Sarac et al. (2016) reported experimental measurement of the discontinuous boundaries between plastic slip sectors based upon measurements of the β-field.

In principle, **B** can be determined by taking a Burgers circuit on an atomic-resolution Transmission Electron Microscopy (TEM) image to measure the $\mathbf{b}^p_{net}$ introduced by discrete dislocations. Alternately **B** can be determined using continuum-based concepts from the relationship

$$\mathbf{B} = \alpha \cdot \boldsymbol{\ell}, \tag{1}$$

where α is the Nye dislocation density tensor and ℓ is the unit normal vector to the atomic plane that contains the Burgers circuit, Γ, taken in a right-hand sense. The Nye tensor is a non-symmetric and second rank tensor.

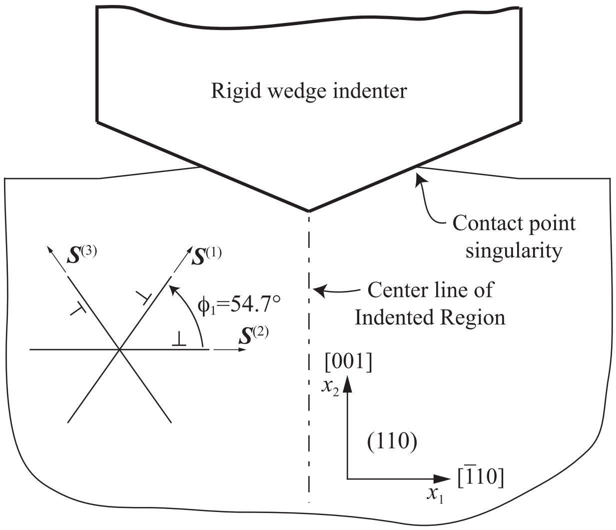

Fig. 2. Schematic representation of wedge indention of single FCC crystal under plane strain conditions. The orientations of the three effective in-plane plastic slip systems and the contact point singularities are indicated (Saito and Kysar, 2011).

2.1. Specimen and crystallography

The experimental specimen used in this study is a nickel face-centered cubic (FCC) single crystal shown schematically in Fig. 2 in its undeformed reference configuration with crystallographic direction [$\bar{1}$10] parallel to the horizontal x_1-axis, [001] parallel to the vertical x_2-axis and [110] parallel to the out-of-plane x_3-axis. A wedge indenter with a 90° included angle impinges into the crystal from above; the wedge axis is parallel to [110]. The orientations of the specimen and the wedge were chosen to induce plane strain deformation in (110) crystallographic planes under conditions of *small scale yielding*, at least away from out-of-plane free surfaces. For such a plane strain deformation state, the Nye dislocation density tensor has two non-zero components, both of which can be measured unambiguously (Kysar et al., 2010). Furthermore when ℓ is taken to coincide with the out-of-plane direction (i.e. the [110]), the Net Burgers Density Vector, **B**, lies within the plane of deformation. We indicate the direction of **B** within the (110) plane by the angle β measured relative to the x_1-axis.

Under these conditions the ⟨110⟩{111} slip system family reduces to six slip systems activated in pairs that induce in-plane plastic deformation in the three directions indicated in Fig. 2. Following Rice (1987) we refer to these as in-plane *Effective Slip Systems* and following Kysar et al. (2005) we label the effective slip systems as 1, 2 and 3. As described in detail by Kysar et al. (2005), effective slip system 1 is a co-planar pair of slip systems with effective unit slip direction $\mathbf{S}^{(1)}$ oriented at an angle of $\phi_1 = \arctan\sqrt{2} \approx 54.7^\circ$ relative to the x_1-axis. Effective slip system 2 is a co-linear pair of slip systems with effective unit slip direction $\mathbf{S}^{(2)}$ oriented parallel to the x_1-axis. Effective slip system 3 is a co-planar set of slip systems with effective unit slip direction $\mathbf{S}^{(3)}$ oriented at an angle of $\phi_3 = \pi - \arctan\sqrt{2} \approx 125.3^\circ$ relative to the x_1-axis. Due to the plane strain conditions, plastic slip on each effective slip system can be thought of as being induced by an effective edge dislocation with unit line direction, $\mathbf{T}^{(i)}$, where i indicates effective slip system number. The effective edge dislocations are each shown in their "positive" senses in Fig. 2. For all three effective slip systems, $\mathbf{T}^{(i)}$ coincides with [110] which is parallel to the x_3-axis. The unit slip plane normals, $\mathbf{N}^{(i)}$, of the effective slip systems are given by $\mathbf{N}^{(i)} = \mathbf{T}^{(i)} \times \mathbf{S}^{(i)}$.

As explained in Kysar et al. (2005) and shown in Fig. 3, the yield surface is a hexagon in Mohr's circle stress space with $(\sigma_{11} - \sigma_{22})/2\tau$ on the abscissa and σ_{12}/τ on the ordinate. Here we assume a fully annealed crystal so the critical shear stress, τ, is the same for each slip system. Two opposite and parallel sides of the hexagon express the yield condition for each of the effective in-plane slip systems. As the slip systems harden the critical shear stress of each individual slip system increases which causes the respective yield surface facets to move away from the stress space origin, thus distorting the yield surface. Furthermore the entire yield surface rotates in stress space as the crystal lattice rotates due to plastic deformation.

After plastic deformation is induced via wedge indentation, the specimen is cut along a center-section with a wire Electrical Discharge Machine (EDM) to expose a (110) surface that suffered plane strain deformation. As described in Kysar et al. (2010), the newly exposed surface is electrochemically polished to remove any material deformed during the EDM process. Spatially resolved measurements (Ruggles et al., 2016) of the as-deformed orientation of the crystal lattice were made using High-Resolution Electron Backscatter Diffraction (HR-EBSD). The two non-zero components of the Nye dislocation density tensor were determined from the HR-EBSD measurements while neglecting the elastic strain of the crystal lattice. Thus the Nye dislocation density tensor is fully characterized experimentally.

The Nye dislocation density tensor can be processed in two complementary and equivalent ways. The first is to calculate the lower bound on the total GND density (i.e. the sum of the absolute values of the GND densities on individual slip

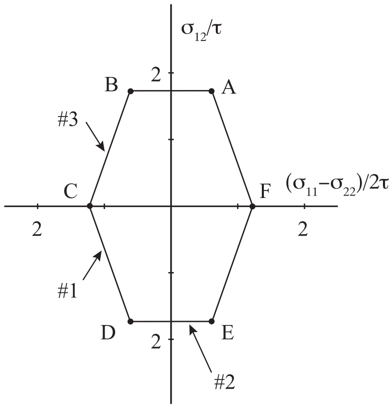

Fig. 3. Yield surface for face centered cubic crystal plastically deformed in plane strain deformation in the (110) crystallographic plane.

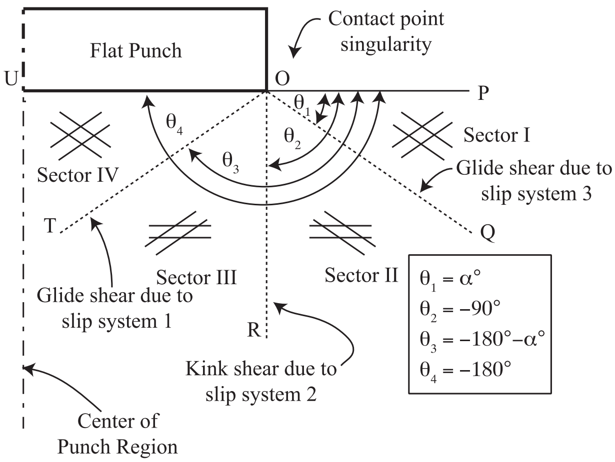

Fig. 4. Asymptotic deformation and stress fields near the contact point singularity of a flat punch. The angle α indicates the orientation of effective slip system 1, which for a FCC crystal is $\alpha \approx 54.7°$ (Kysar et al., 2005).

systems) on the three effective in-plane slip systems as discussed in Kysar et al. (2010). The second is to calculate **B** as discussed above in Eq. (1). We will focus on the latter calculation in this study because **B** – through its direction β – can be used to determine the boundaries between plastic slip sectors and as a consequence can serve as a validation measure for single crystal plasticity constitutive relations.

3. Plastic deformation fields due to wedge indentation

Before discussing the experimental results, we first consider theoretical predictions of the plastic deformation under the wedge indenter. The specimen geometry, plastic slip systems and loading all have mirror symmetry about the center line of the indented region shown in Fig. 2. Hence we need only to consider the deformation on the right side of the center line. The angled indenter first comes into contact with the specimen at its tip along the center line. The portion of the wedge in contact with the material increases in length as indentation proceeds.

There exists a well-known analogy between a flat punch impinging on a surface and a stationary crack tip in a material based upon the similarity between boundary conditions. Asymptotic analyses show that a singularity in deformation measures and/or stress exists at the edge (or line) of a flat punch, which we refer to in cross-section as a *Contact Point Singularity*. Rice (1973) showed that the asymptotic field at the edge of a flat punch in a single crystal consists of constant stress angular plastic slip sectors centered at the contact point singularity. One or two effective in-plane slip systems are active within each constant stress angular sector. The boundaries between the angular slip sectors are rays emanating from the contact point singularity, across which the stresses and deformation measures can change discontinuously.

The asymptotic deformation field at the contact point singularity of a flat punch for the crystallographic orientation considered herein is shown in Fig. 4, where for a FCC crystal the orientation of effective in-plane slip system is $\alpha = \tan^{-1}\sqrt{2} \approx 54.7°$. The asymptotic deformation field consists of four angular plastic slip sectors labelled as I, II, III and IV. The active slip systems within each sector are indicated schematically. The velocity, stress and active slip systems change

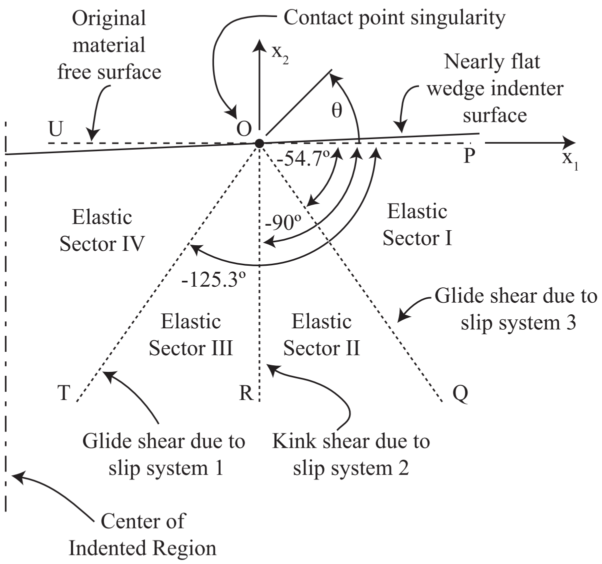

Fig. 5. Asymptotic deformation and stress fields near the contact point singularity of a nearly-flat wedge indenter (Saito and Kysar, 2011; Saito et al., 2012).

discontinuously across the boundaries between the angular slip sectors. As described by Rice (1987), dislocations act in "glide" shear mode at the boundaries between sectors I and II as well as between III and IV. At boundary between sectors II and III, the dislocations are predicted to manifest themselves in "kink" shear mode.

For a wedge indenter, the contact point singularity coincides with the point where the wedge loses contact with the material. As indentation proceeds, the contact point singularity propagates along the surface of the material away from the center line as indicated in Fig. 2. The indentation-fracture analogy must be generalized to account for the propagating contact point singularity, which results in asymptotic fields that correspond to those of a quasistatically moving (and closing) crack tip. A similar asymptotic angular sector structure exists with its center at the contact point singularity, and the asymptotic structure follows the contact point singularity as it propagates along the specimen surface. However the asymptotic behaviors associated with a stationary contact point singularity and a propagating contact point singularity have very different forms.

Drugan and Rice (1984) and Drugan (1986) demonstrated that a surface of discontinuity propagating within a material that satisfies the maximum plastic work inequality can not have discontinuities in stress, but discontinuities in velocity are admissible. As a consequence of this limitation, the asymptotic angular sector structure associated with a quasistatically moving contact point singularity must contain elastically deforming angular sectors. Rice (1987) derived the asymptotic fields for a quasistatically growing crack in a single FCC crystal of the orientation shown in Fig. 2. Saito and Kysar (2011) applied the same concepts to derive the asymptotic deformation fields beneath the contact point singularity of a nearly-flat (i.e. included angle approaching 180°) wedge indenter of the orientation shown in Fig. 2. The asymptotic fields, shown in Fig. 5 again contain four angular sectors separated by radial boundaries emanating from the contact point singularity. The three radial boundaries between the angular sectors are at the same angles as the radial boundaries predicted for the flat punch in Fig. 4. In addition, the active slip systems and dislocation structures at the three radial boundaries are predicted to be the same as for the asymptotic fields associated with the flat punch. However for the nearly-flat wedge, the material instantaneously within each of the four angular sectors deforms elastically whereas for a flat punch the material within the four angular sectors deforms plastically.

Saito et al. (2012) performed detailed single crystal plasticity FEM simulations of wedge indentation to investigate the extent that the asymptotic fields extend into the material assuming an elastic ideally-plastic constitutive relationship. Fig. 6a shows the results for a nearly-flat wedge indenter; the simulation domain is the material to the right of the center line of the indented region just as in Fig. 5. The length scale a is the instantaneous distance of the contact point singularity from the center line of the indented region. Thus the contact point singularity is at $x_1/a = 1$ as indicated by a small black circle. The FEM simulation predictions of the total plastic strain rate, non-dimensionalized as $\dot{\gamma}_{tot}a/\dot{a}$, where the over-dot indicates differentiation with respect to time, demonstrate the same asymptotic field as the analytical predictions in Fig. 5. Specifically four angular instantaneously elastically deforming sectors separated by rays of plastically deforming material propagate through the material along with the contact point singularity. The angular sector structure extends into the material far beyond the regime of validity of the equations that govern the asymptotic behavior.

Fig. 6b shows single crystal plasticity FEM predictions of the non-dimensionalized total plastic strain rate due to indentation of a rigid wedge with a 90° included angle; again only the right half of the deforming domain is shown. The asymptotic structure of rays of plastic deformation separated by angular sectors of elastic deformation is observed despite

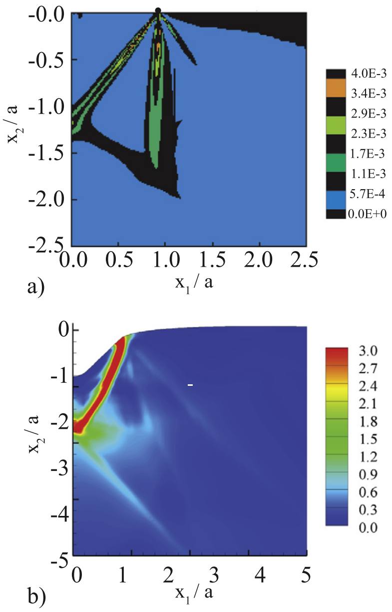

Fig. 6. Dimensionless total plastic strain rate, $\dot{\gamma}_{tot}\, a/\dot{a}$, in FCC crystal as a consequence of (a) indentation with a nearly-flat wedge, and (b) indentation of wedge with 90° included angle. The over dot indicates differentiation with respect to time and a represents the distance between the contact point singularity and the center line of the indented region (Saito et al., 2012).

the very large deformations and lattice rotations. Specifically, the ray of glide shear on effective slip system 1 (cf. Fig. 2) extends from the contact point singularity to the center line of the domain, however in the case of finite deformation, the slip planes have developed a noticeable curvature. Likewise, the ray of kink shear on effective slip system 2 and the ray of glide shear on effective slip system 3 both persist in the case of finite deformations, but their directions are affected by the finite lattice rotations. The rays of plastic deformation separate angular sectors of elastically deforming material close to the contact point singularity. However this asymptotic structure extends into the materials a distance only of about a. Beyond that distance the simulations predict extensive plastic deformation occurring within the angular sectors. Thus the deformation fields transition from an asymptotic field suitable for a moving contact point singularity to one suitable for a stationary contact point singularity at radii greater than a.

The overall plastic deformation fields are established by the integrated plastic strain rate fields that propagate quasistatically through the material. As will be described in detail below, the deformation fields are divided into plastic slip sectors within which well-defined slip systems or sets of slip systems are active. The locations of the boundaries between the plastic slip sectors are a function of the constitutive relationships that determine the rate of hardening of the individual slip systems. Experimentally we can characterize the plastic slip sectors and their boundaries with measurement of the Net Burgers Density Vector, **B**, as well as the associated β-field (Sarac et al., 2016), which establishes a methodology for the experimental validation of elastic-plastic constitutive relationships.

4. Finite element simulations

The elastic-plastic behavior of a nickel single crystal through a wedge indentation process was simulated based upon single crystal plasticity and the finite element method. The FEM simulations were conducted using a commercial software (ABAQUS/Standard, v.6.10) while employing a user-material subroutine (UMAT) for single crystal plasticity written by Huang (1991) and modified by Kysar (1997). The specimen configuration, crystallographic orientation and loading configuration are shown in Fig. 2. The wedge indenter with a 90° included angle with a tip radius of curvature of 100 µm was treated as a rigid body. Due to mirror symmetry of the specimen, crystallographic orientation and loading about the vertical line through the indenter tip, we modeled only the right half of the domain shown in Fig. 2. Plane strain bilinear four-node quadrilateral reduced integration elements were used to simulate the plane strain deformation state of the material that exists away from the specimen free edges. The material near the contact region – where extreme plastic deformations occur – had a much higher mesh density than material away from the contact region.

We employed a classical phenomenological constitutive hardening relationship, which is referred to as the Peirce–Asaro–Needleman (PAN) model (Peirce et al., 1982; 1983), to demonstrate the effectiveness of using the measured β-field to validate choices of constitutive parameters. We purposedly choose this classical constitutive model because of the straightforward physical interpretations of the constitutive parameters.

Table 1
Sets of hardening parameters employed with the PAN constitutive hardening model. Latent hardening ratio q varies between 1 and 1.6. Saturation stress τ_s and the initial hardening modulus h_0 are normalized by the initial yield stress τ_0.

Simulation #	q	τ_s/τ_0	h_0/τ_0
1	1.0	5	10
2	1.0	5	1
3	1.0	2	10
4	1.0	2	1
5	1.2	5	10
6	1.4	5	10
7	1.6	5	10

Hill (1966) proposed that the plastic constitutive hardening rate in a plastically deforming single crystal can described as

$$\dot{\tau}^{(\alpha)} = \sum_{\beta=1}^{N} h_{\alpha\beta}\dot{\gamma}^{(\beta)}, \tag{2}$$

where N is the total number of slip systems, $\dot{\tau}$ is the hardening rate of each slip system α, $\dot{\gamma}$ is the slip rate and $h_{\alpha\beta}$ is the hardening moduli matrix. The hardening moduli matrix is determined by the phenomenological hardening models. Peirce et al. (1982) postulated a functional form for the current resolved shear stress, denoted as τ, on single slip system that can be fit to experiment and is given by

$$\tau^{(\alpha)} = \tau_0 + (\tau_s - \tau_0)\tanh\left(\frac{h_0\gamma^{(\alpha)}}{\tau_s - \tau_0}\right). \tag{3}$$

where γ is the plastic slip on the slip system, τ_0 is the initial critical resolved shear stress (i.e. $\tau_0 = \tau^{(\alpha)}(0)$), τ_s is the saturation stress, and h_0 is the initial hardening modulus (i.e. $h_0 = h(0)$). The hardening behavior of the single crystal is determined by a hyperbolic tangent function as shown in Fig. 8.

The hardening moduli that are used in PAN hardening model are

$$h_{\alpha\alpha} = h(\gamma) = h_0\,\mathrm{sech}^2\left|\frac{h_0\gamma}{\tau_s - \tau_0}\right|, \tag{4a}$$

$$h_{\alpha\beta} = qh(\gamma) \quad (\alpha \neq \beta), \tag{4b}$$

where $h(\gamma)$ is the derivative of resolved shear stress with respect to shear strain (i.e. $h(\gamma) = d\tau/d\gamma$), $h_{\alpha\alpha}$ term is the *self-hardening modulus*, $h_{\alpha\beta}$ (for $\alpha \neq \beta$) is the *latent hardening modulus* and q is the latent hardening ratio. The latent hardening ratio is described as the ratio of the latent hardening rate to the self hardening rate of a slip system. The total accumulated strain on all slip systems is calculated as

$$\gamma = \sum_{\alpha=1}^{N}\int_0^t |\dot{\gamma}^{(\alpha)}|dt. \tag{5}$$

Table 1 lists seven sets of parameters used in this study for the PAN model. Thus seven simulations were performed to capture the effect of the hardening parameters on plastic slip sectors and their boundaries as identified by the β-fields. The other classical phenomenological constitutive hardening relationship is the Bassani–Wu (BW) model (Bassani and Wu, 1991; Wu et al., 1991) which has three additional parameters. The effect of its parameters on plastic slip sectors and their boundaries identified by the β-fields will be investigated in another study.

5. Results and discussion

We first consider the plastic slip sectors that manifest themselves in plastically deforming zone for PAN hardening model. Fig. 7 indicates the regions within which various effective plastic slip systems or sets of effective plastic slip systems are responsible for more than 95% of the plastic slip. We can rationalize the spatial sequence of the plastic slip sectors by considering known stress states in the context of the yield surface in Fig. 3.

Upon noting the mirror symmetry of the specimen, crystallographic orientation and the loading about the vertical line through the indenter tip, as seen in Fig. 2, it is clear that the shear stress component on the vertical symmetry line has value $\sigma_{12} = 0$. In addition, given the compressive loading, we know that $\sigma_{22} < 0$. Therefore early in the indentation process when the lattice rotation is negligible, we expect the stress state of material points along the vertical symmetry line to be at vertex F of the yield surface in Fig. 3, thus satisfying the yield criteria for both effective slip systems 1 and 3. Similarly the stress components on the horizontal traction free surface to the right of the contact point singularity include $\sigma_{12} = 0$

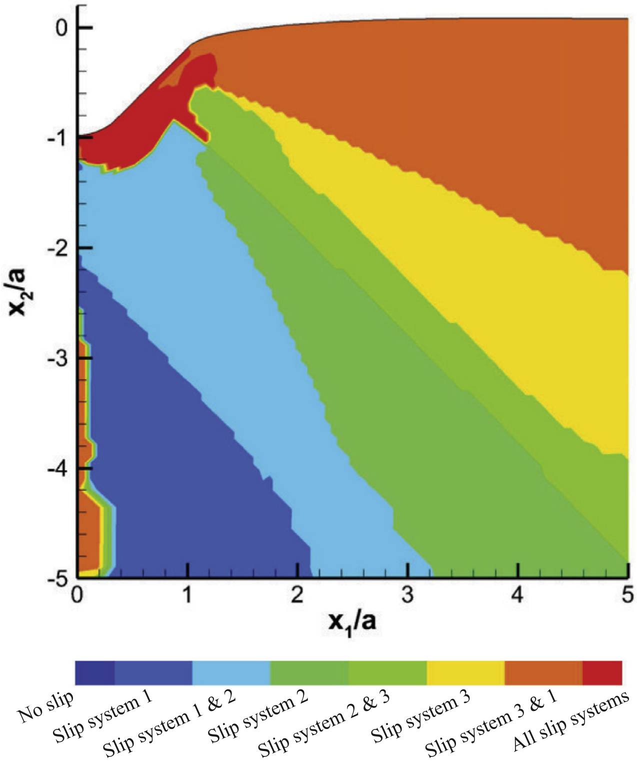

Fig. 7. Slip sectors associated with plastic deformation due to wedge indentation. The contours indicate regions within which the indicated effective in-plane slip systems are responsible for more than 95% of the plastic slip (Dahlberg et al., 2014).

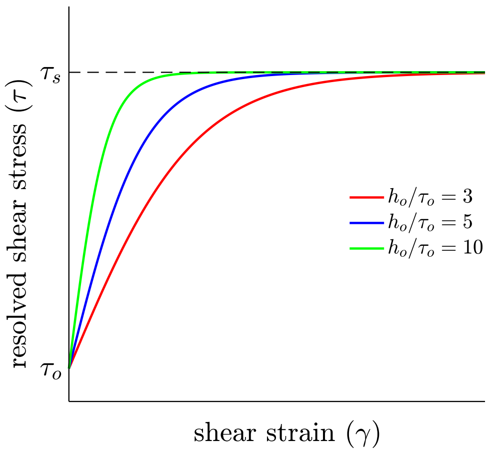

Fig. 8. Stress vs. Strain relationship according to PAN model.

and $\sigma_{22} = 0$, with $\sigma_{11} < 0$. Thus, if plastic deformation occurs at the horizontal traction free surface, the stress state must be at vertex C of the yield surface, again satisfying the yield criteria for both effective slip systems 1 and 3. As can be seen in Fig. 7, there is a plastic slip sector in the form of a narrow strip on the vertical symmetry line within which effective slip systems 1 and 3 are active. Similarly, there is a large plastic slip sector near the horizontal traction free surface within which effective slip systems 1 and 3 are active.

Fig. 9 shows the spatial distribution of β, which we refer to as the β-field. The value of β at each material point is calculated from the predicted crystal lattice rotation using the methodology described in Kysar et al. (2010) and Sarac et al. (2016). It is evident that the plastic slip sectors in Fig. 7 correspond closely to various sectors of the β-field in Fig. 9. As a consequence, the measured β-field provides a means of experimentally identifying the plastic slip sectors, as discussed in Kysar et al. (2010); Sarac et al. (2016).

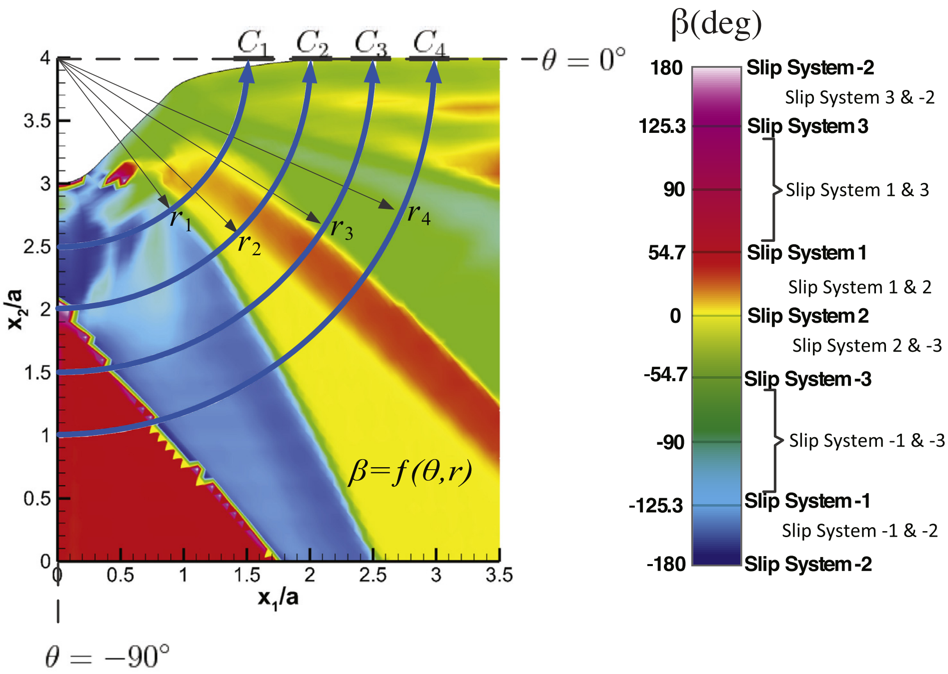

Fig. 9. Predicted spatial distribution of β-variable.

We now consider the material points between the vertical symmetry line and the horizontal traction free surface. Fig. 9 shows four circular arcs centered at the point on the material where the indenter tip first made contact. The circular arcs are labeled C_1, C_2, C_3 and C_4, that have radii of $r_1 = 1.5a$, $r_2 = 2a$, $r_3 = 2.5a$, and $r_4 = 3a$, respectively. The angular position along the arcs relative to the vertical symmetry line is denoted by θ, with $\theta = -90°$ on the vertical symmetry line and $\theta = 0°$ on the traction-free surface.

We first consider arcs C_3 and C_4 because they pass through material that has experienced negligibly small lattice rotations. The arcs pass through a sequence of plastic slip sectors in going from the vertical symmetry line to the horizontal traction free surface. The trajectory in stress space must follow the yield surface if the plastic deformation occurs at all material points along the arcs. It is evident from the applied loading that $\sigma_{12} > 0$ along the arcs so the trajectory in stress space will follow the upper half of the yield surface.

For material points on arcs C_3 and C_4 slightly away from the vertical symmetry line, the stress state leaves vertex F and traverses the facet that connects vertices F and A of the yield surface in Fig. 3, which corresponds to the yield criterion for effective slip system 1. This explains the existence of the plastic slip sector for effective slip system 1 in Fig. 7. Moving further counterclockwise along the arcs, the stress state reaches vertex A of the yield surface, for which both effective slip systems 1 and 2 are activated simultaneously, consistent with Fig. 7. Next is a plastic slip sector within which only effective slip system 2 is activated, which corresponds to the yield surface facet joining vertices A and B. The existence of remaining plastic slip sectors can be rationalized in a similar manner until the stress state arrives at vertex C on the traction free surface as discussed above.

Material points on circular arcs arcs C_1 and C_2 are sufficiently close to the indenter that significant lattice rotation has occurred due to plastic deformation which affected the active slip systems. As shown in Fig. 6b and discussed by Saito et al. (2012), the intense ray of plastic deformation on effective slip system 1 extending from the contact point singularity to the vertical symmetry line introduces significant rotation of the crystal lattice. Since the stress space is Mohr's circle stress space, any rotation of the crystal lattice leads to double the rotation of the yield surface in stress space (e.g. Kysar et al., 2005). Hence, on the vertical symmetry line where $\sigma_{12} = 0$ the crystal lattice rotates until vertex A of the yield surface is coincident with the abscissa of the stress space, upon which both effective slip systems 1 and 2 are activated along the vertical symmetry line.[1] Thus the plastic slip sector within which both effective slip systems 1 and 2 are activated starts at the vertical symmetry line near the indenter tip and extends down into the material into the region discussed above.

Sarac et al. (2016) reported experimental measurements of the β-fields in a single nickel crystal shown in Fig. 10(a). The high spatial frequency variation in the β-field corresponds to dislocation cell structure and the low spatial frequency variations correspond to the plastic slip sectors that form as a consequence of the continuum single crystal plasticity boundary

[1] As a consequence, the maximum magnitude of lattice rotation is expected to be a constant value near the vertical symmetry line in this region. This is observed experimentally in Kysar et al. (2010).

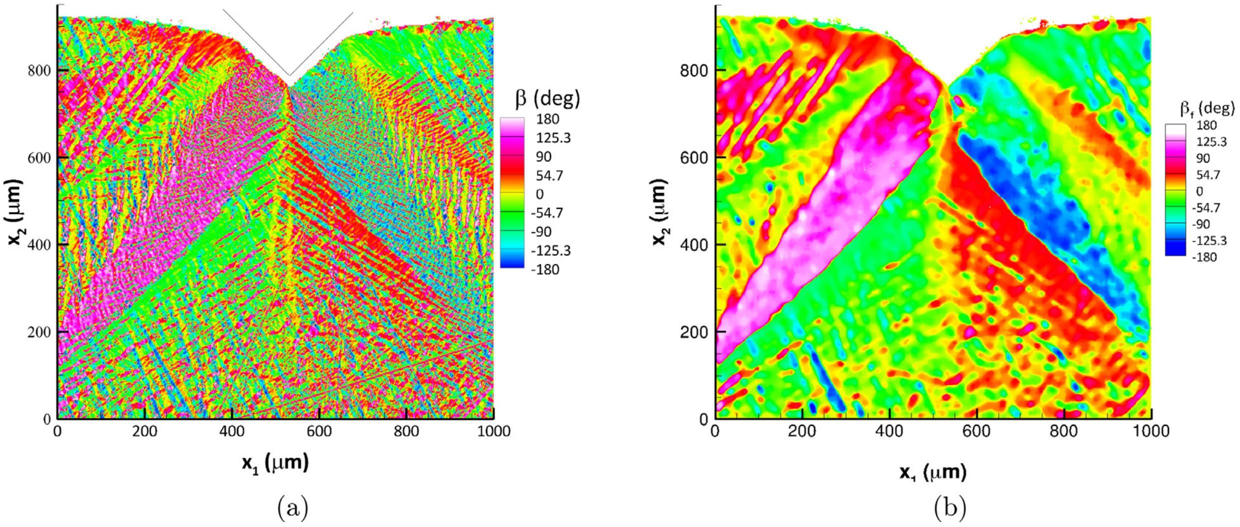

Fig. 10. Experimental measurements of β-fields: (a) As-measured experimental β-field; (b) 2D filtered experimental β-field.

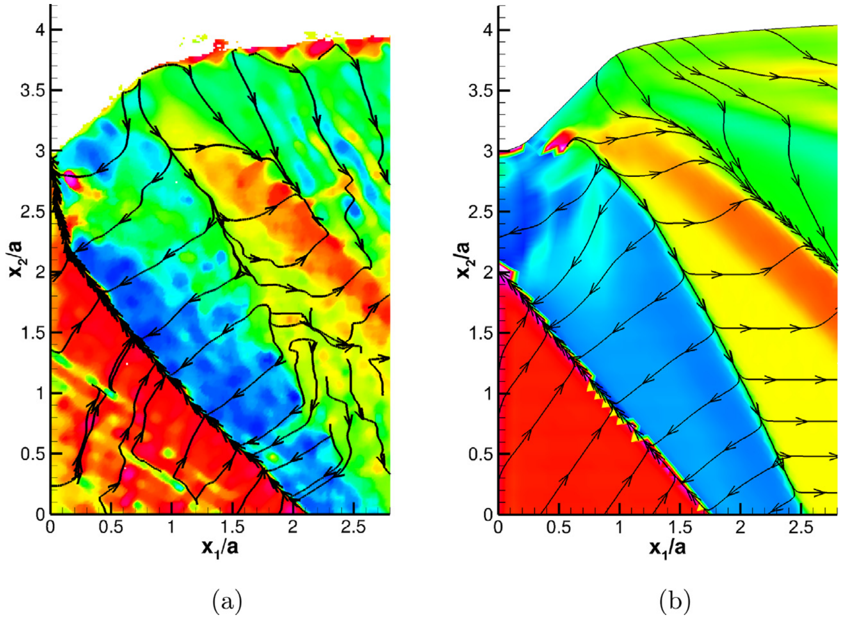

Fig. 11. The β-fields showing spatially resolved directions of the Net Burgers Density Vector: (a) Experimental; (b) PAN Simulation#7.

value problem. Since the classical constitutive hardening relationships do not account explicitly for the formation of dislocation cell structures, Sarac et al. (2016) performed a low-pass filter of the β-field with the results shown in Fig. 10(b) to facilitate comparison with numerical continuum predictions. Finally, Sarac et al. (2016) demonstrated that the boundaries between the various sectors of the β-field (i.e. discontinuities in active slip systems) can be readily delineated by integrating the directions of **B** to calculate the trajectories of the β-field (i.e. curves instantaneously tangent to **B** at each material point). Fig. 11(a) shows the experimental results of the filtered β-field overlaid with the **B** trajectories and Fig. 11(b) shows corresponding numerical predictions. A qualitative comparison indicates close correspondence between the experiments and numerical predictions. In the remainder of this Section we perform a quantitative comparison as a means of experimental validation of the constitutive parameters of the PAN hardening model.

In the first part of what follows we present plots of β as a function of angle along arcs C_1, C_2, C_3, and C_4 as shown in Fig. 9. In particular we will look at the effect of the various constitutive parameters on the predicted variation β with θ. In the second part of the analysis we probe, respectively, the relationships between γ vs. θ and $\dot{\gamma}(a/\dot{a})$ vs. θ to determine the variations of the plastic strains and slip rates associated with each slip system. In the third part of the analysis we present the stresses plotted in the stress space in order to probe the stress state within the plastic slip sectors.

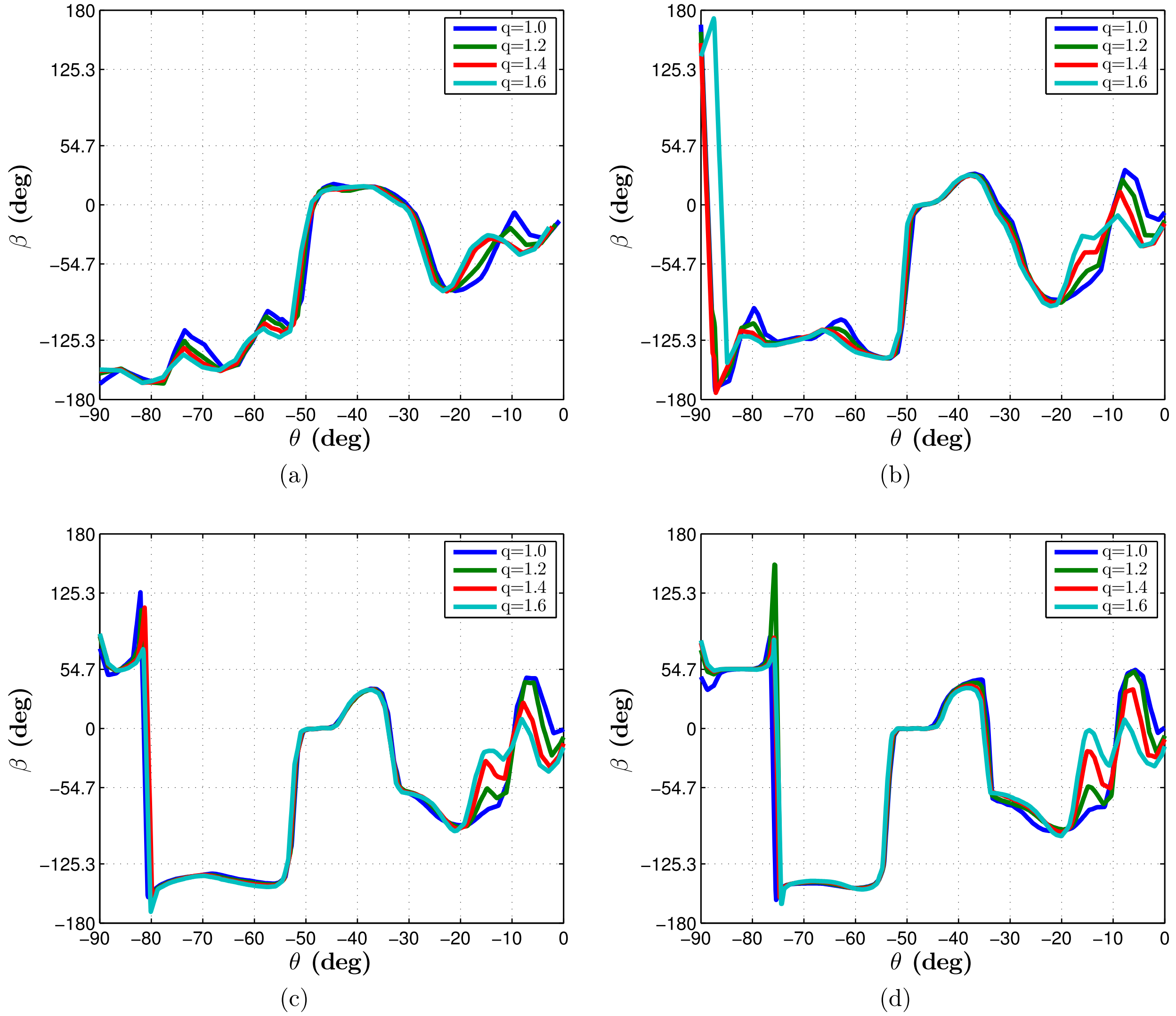

Fig. 12. Effect of latent hardening ratio, q, on β using PAN constitutive parameters $\tau_s/\tau_0 = 5$, and $h_0/\tau_0 = 10$: (a) β as a function of θ along C_1; (b) β as a function of θ along C_2; (c) β as a function of θ along C_3; (d) β as a function of θ along C_4.

5.1. Effects of constitutive parameters on β

To explore the effects of constitutive parameters on β, the plots of β vs. position as a function of constitutive parameters are presented. The position is given ranging from -90° to 0°. The value of β on each ordinate ranges from -180° to 180° with demarcations at the slip orientation angles of -125.3°, -54.7°, 0°, 54.7°, 125.3° and 180°. The active slip systems change as β moves vertically across these demarcation lines as discussed in Kysar et al. (2010) and Sarac et al. (2016) as well as in Fig. 9.

5.1.0.1. Effect of latent hardening ratio. The results from four simulations are compared to explore the influence of the latent hardening ratio, q, on the β-variable using the PAN constitutive model. Since the parameters other than the latent hardening parameter are identical for the PAN Simulations #1, #5, #6, and #7, these four simulations are employed to make the comparisons. The constitutive parameters employed are $\tau_s/\tau_0 = 5$, and $h_0/\tau_0 = 10$ while the latent hardening parameter is varied from 1.0, 1.2, 1.4 to 1.6.

It can be observed that the latent hardening ratio, q, does not significantly affect the β-variable as shown in Fig. 12 and, accordingly, it does not affect the positions of plastic slip sector boundaries. This is expected because as shown in Fig. 7 previously latent plastic slip systems are activated in only a small region near the indenter tip, so the value of q affects the deformation only in that region. However, some changes in β can be observed at θ between 0° and -20° near the traction free surface where extreme plastic deformation is not expected. This behavior is investigated later by probing the stress space along the arcs in order to analyze the elastic-plastic behavior of the single crystal.

5.1.0.2. Effect of initial hardening modulus. We now explore the influence of the initial hardening modulus, h_0, on the β-variable using the PAN constitutive model. Simulations #1 and #2 both use saturation stress, $\tau_s/\tau_0 = 5$ and latent hardening is $q = 1.0$ with values of h_0/τ_0 of 10 and 1, respectively. The vertical jumps in β indicate the boundaries between plastic slip sectors. The angular position at which this jump occurs changes (see On-Line Supplementary Information for the figure associated with the effect of initial hardening modulus,h_0, on β using PAN constitutive parameters with $\tau_s/\tau_0 = 5$, and $q = 1.0$). Thus the positions of boundaries between the plastic slip sectors are sensitive to the hardening rate. Angular boundary shifts of about 5° are seen at the radii associated with C_1, C_2, C_3 and C_4.

We also explore the effect of the initial hardening modulus by comparing the PAN simulations #3 and #4, in which the saturation stress ratios $\tau_s/\tau_0 = 2$ and latent hardening ratio $q = 1.0$ with values of h_0/τ_0 of 10 and 1, respectively. The changes in β are smaller than before and thus the boundaries of the slip activity regions remained nearly the same (see On-Line Supplementary Information for the figure associated with the effect of initial hardening modulus,h_0, on β using PAN constitutive parameters with $\tau_s/\tau_0 = 2$, and $q = 1.0$).

The differences between the cases can be attributed to the fact that the β-fields in the first case are still evolving (i.e. the slip system strength differs from one material points to the next) because of the high value of $\tau_s/\tau_0 = 5$. On the other hand, the β-fields in the second case have converged to steady-state behavior because with $\tau_s/\tau_0 = 2$ all the slip system strengths at almost all (except perhaps near the traction-free surface) material points has saturated. This is especially the case for $h_0/\tau_0 = 10$ (see On-Line Supplementary Information).

5.1.0.3. Effect of saturation stress. We next consider the effect of τ_s on the behavior of β based upon the constitutive parameters $h_0/\tau_0 = 10$ and $q = 1.0$ in PAN simulations #1 and #3 with corresponding values for the saturation stresses are τ_s/τ_0 equal to 2 and 5. The saturation stress has a strong influence on the β-variable and therefore on the positions of the boundaries separating plastic slip sectors (see On-Line Supplementary Information for the figure associated with the effect of saturation stress).

5.2. Plastic slip and plastic slip rates

Sarac et al. (2016) showed that the β-fields obtained from FEM simulations using the PAN constitutive relationship are in qualitative agreement with experiment for certain sets of constitutive parameters, specifically PAN #6 and #7 (cf. Table 1). We now report the plastic slip and plastic slip rate as a function of angular position along the circular arcs from these simulations.

Fig. 13 shows the plastic slip on each effective slip system (respectively, $\gamma^{(1)}$, $\gamma^{(2)}$, and $\gamma^{(3)}$) upon employing the PAN constitutive parameter set #6 with $q = 1.4$, $\tau_s/\tau_0 = 5$ and $h_0/\tau_0 = 10$. Total plastic slip along the arcs were calculated $\gamma_{total} = \gamma^{(1)} + \gamma^{(2)} + \gamma^{(3)}$. The normalized plastic slip rates were obtained pertaining to the parameter set #6 to show the degree of plastic slip – if any – occurring at the peak indentation load (see On-line Supplementary Information). The plastic slip rates are normalized by the quantity $\dot{a}/a$. The instantaneous boundaries between the plastic slip sectors can be inferred from these results. The variation of the normalized slip rates along C_4 reveals six regions whose boundaries are determined by the range of the θ angle. The ranges of θ for the boundaries of the regions denoted I, II, III, IV, and V are $[-90^\circ, -78^\circ]$, $[-78^\circ, -52^\circ]$, $[-52^\circ, -38^\circ]$, $[-38^\circ, -35^\circ]$, and $[-35^\circ, -10^\circ]$, respectively (see On-Line Supplementary Information). The material deforms elastically in the region around $\approx -5^\circ$. Therefore, only effective slip system 1 is active in plastic slip sector I, effective slip system 1 and effective slip system 2 are active together in plastic slip sector II, only effective slip system 2 is active in plastic slip sector III, effective slip system 2 and effective slip system 3 are active together in plastic slip sector IV, and only effective slip system 3 is active in plastic slip sector V. The plastic slips were obtained employing the PAN constitutive parameter set #7 with $q = 1.6$, $\tau_s/\tau_0 = 5$ and $h_0/\tau_0 = 10$. The normalized slip rates associated with parameter set #7 were also obtained to discern the slip activity regions (see On-line Supplementary Information). It is evident that the plastic slip sector boundaries are very similar to those from PAN simulation #6. The only difference between the parameters of two simulations is the latent hardening ratio. The slip and the slip rate variations reveal that the latent hardening ratio has a very small influence on the slip activity regions and their boundaries because the latent slip systems are activated only very near the indenter tip.

5.3. Yield surface analysis

Fig. 3 shows the polygonal yield surface of a single FCC relative to the crystallographic orientation in Fig. 2. The stress space has $(\sigma_{11} - \sigma_{22})/2$ on the abscissa and σ_{12} on the ordinate (e.g. Rice, 1973; 1987). The yield criterion for each of the three effective slip systems is given by

$$\sigma_{12} = \tan 2\phi \left[\frac{\sigma_{11} - \sigma_{22}}{2}\right] \pm \frac{\lambda\tau}{\cos 2\phi}, \tag{6}$$

where τ is the critical resolved shear stress of the slip system, λ is a geometric factor that accounts for the precise orientations of the crystallographic slip systems relative to the effective slip system, and ϕ is the angle the effective slip system

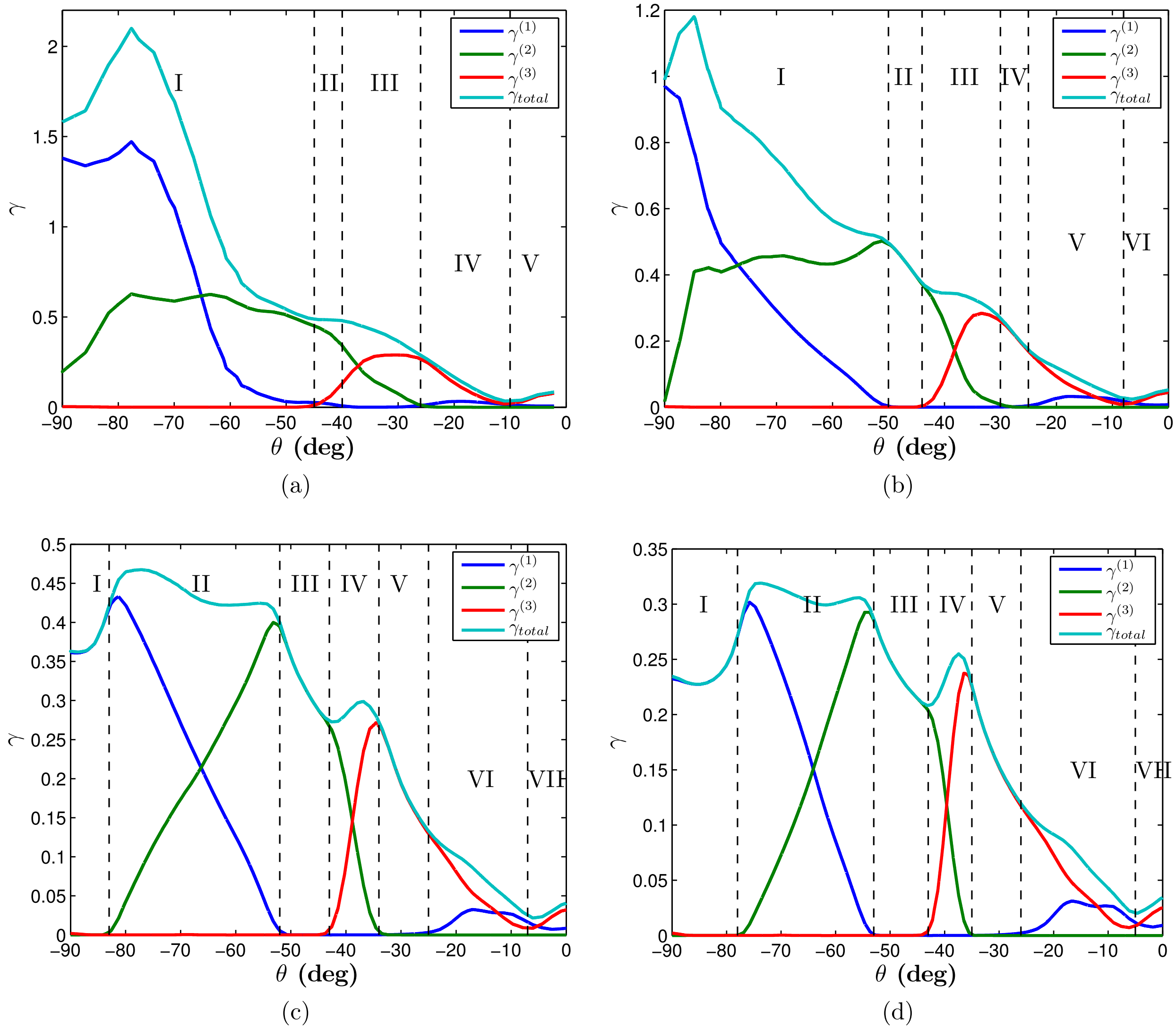

Fig. 13. Total plastic slip, γ_{total} and the plastic slip on each effective slip system $\gamma^{(1)}$, $\gamma^{(2)}$, and $\gamma^{(3)}$ obtained by PAN hardening simulations with $q = 1.4$, $\tau_s/\tau_0 = 5$ and $h_0/\tau_0 = 10$: (a) Plastic strain, γ along C_1; (b) Plastic strain, γ along C_2; (c) Plastic strain, γ along C_3; (d) Plastic strain, γ along C_4.

direction makes with the x_1-axis (Kysar et al., 2005; Rice, 1987). The yield surface is a hexagon because the $\pm$ sign in Eq. (6) defines a set of two parallel lines.

We now plot the stress states along the arcs C_1, C_2, C_3, and C_4 in stress space with the goal of identifying elastically deforming regions. The stresses expressed in the specimen coordinate frame are first extracted from the simulation results and expressed in a local crystallographic coordinate frame where the local x_1-axis is parallel with the $[\bar{1}10]$ direction. The stress components in the rotated crystallographic coordinate from are then plotted in stress space after normalization with the current yield strength.

Fig. 14 shows the stress trajectory in stress space on C_1 for PAN constitutive parameter sets #1, #5, #6 and #7 (see On-Line Supplementary Information for the stress trajectories in stress space, respectively, on C_2, C_3, and C_4 for PAN constitutive parameter sets #1, #5, #6 and #7). The original yield surface is plotted in each figure to allow determination of the material behavior. Material points for which the stress state lies on the yield surface are undergoing plastic slip on the respective slip systems. Alternatively a material point is undergoing elastic deformation if the stress state lies within the yield surface.

The yield surfaces along C_1, C_2, C_3, and C_4 contain limited information about the deformation and stress state of the material. The material points located at the vertices (A, B, C, D, E, F) of the yield surface, where double slip occurs, cannot be determined. The vertices F, A, B, and C indicate the locations of the double slips, where slip systems 1 and 3, slip systems 1 and 2, slip systems 2 and 3, and slip systems 3 and 1, are activated respectively as shown in Fig. 14. The yield surfaces along C_1, C_2, C_3, and C_4 do not give the yield response of the individual material points, which are located on the arcs.

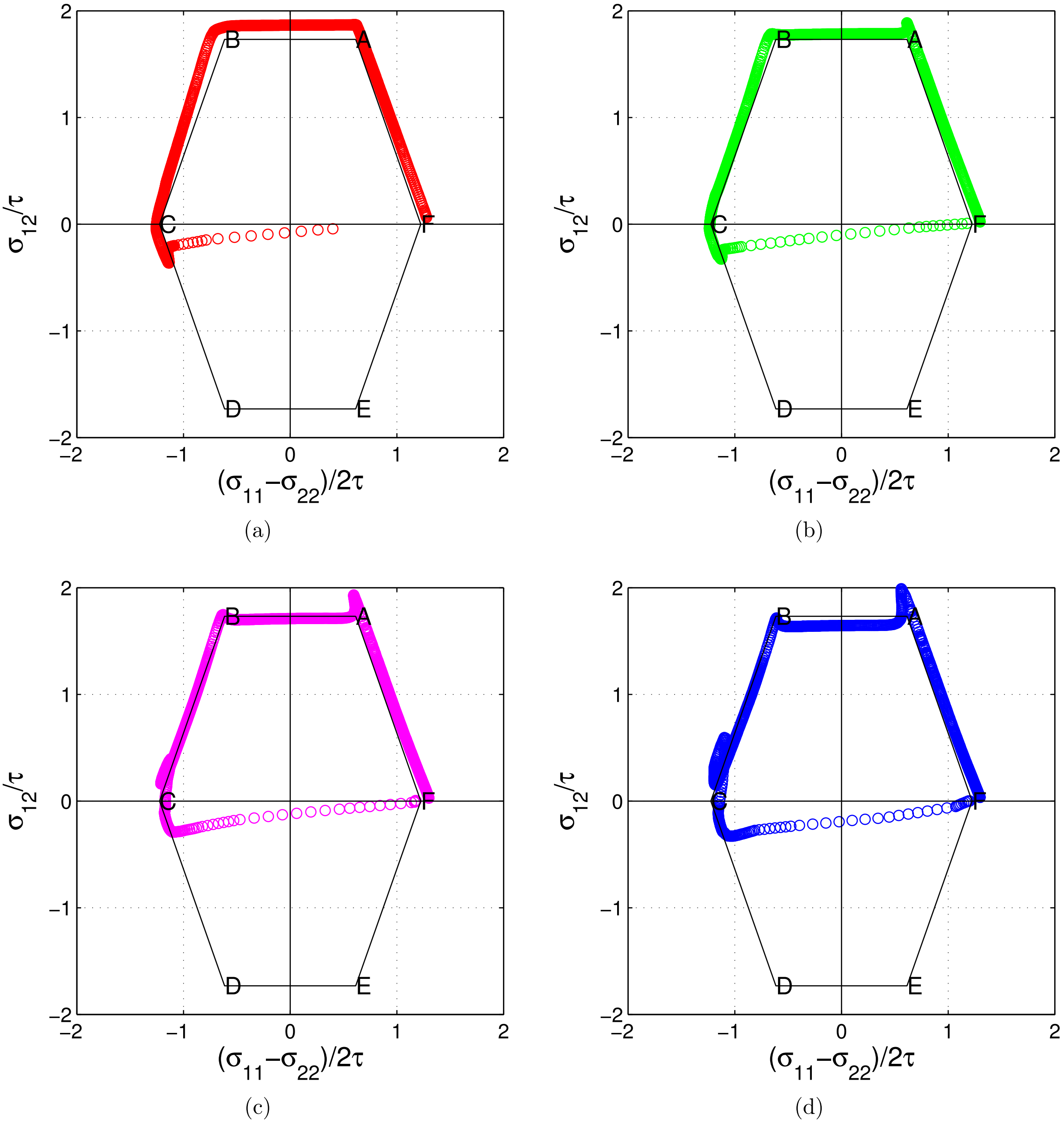

Fig. 14. Yield surfaces along C_1: (a) PAN Simulation#1, where $q = 1.0$, $\tau_s/\tau_0 = 5$, $h_0/\tau_0 = 10$; (b) PAN Simulation#5, where $q = 1.2$, $\tau_s/\tau_0 = 5$, $h_0/\tau_0 = 10$; (c) PAN Simulation#6, where $q = 1.4$, $\tau_s/\tau_0 = 5$, $h_0/\tau_0 = 10$; (d) PAN Simulation#7, where $q = 1.6$, $\tau_s/\tau_0 = 5$, $h_0/\tau_0 = 10$.

In order to get the state of the material points at different θ angles, a new analysis was performed by dividing the yield surface into nine line segments (see On-Line Supplementary Information).

6. Conclusions

In this paper, we present a methodology for experimental validation of single crystal plasticity constitutive relationships based upon spatially resolved measurements of the direction of the Net Burgers Density Vector, which we refer to as the β-field. The β-variable relates information about the active slip systems as well as the ratios Geometrically Necessary Dislocation (GND) densities on the active slip systems. We demonstrate the methodology by comparing single crystal plasticity finite element simulations of plane strain wedge indentations into face-centered cubic nickel to detailed experimental measurements of the β-field. We employ the classical Peirce–Asaro–Needleman (PAN) hardening model in this study due to the straightforward physical interpretation of its constitutive parameters.

The constitutive parameters are the latent hardening ratio, initial hardening modulus and the saturation stress. The saturation stress and the initial hardening modulus have a relatively large influence on the β-variable compared to the latent hardening ratio. A change in the initial hardening modulus leads to a shift in the boundaries of the plastic slip sectors. As the saturation strength varies, both the magnitude of the β-variable and the boundaries of the plastic slip sectors change. We identified a set of constitutive parameters that are consistent with the β-field obtained from the experiment.

The present study also includes a detailed computational analysis of the deformation state of the material by monitoring variations of the plastic slip and plastic slip rates along circular arcs in the plastically deformed region. This analysis confirms that the β-field is able to predict the plastic slip sectors and their boundaries in the plastically deforming region.

Finally, we plot the stress state in stress space to identify regions of elastic deformation. The results show that elastically deforming sectors translate along with plastically deforming sectors as the indentation depth increases. The elastic sectors are a consequence of the maximum plastic work inequality as described by Drugan and Rice (1984) and Drugan (1986) and their presence serves as verification that the finite element simulations were performed correctly.

In closing, we note that this methodology can, in principle, be applied to any arbitrary elastic-plastic deformation state as long as all components of the Nye tensor can be measured experimentally. The EBSD method inherently makes two-dimensional measurements, so any non-zero out-of-plane components of the Nye tensor can typically not be obtained. In this study, we designed the specimen and loading such that all out-of-plane components are zero. For more general deformation states, however, some information about the out-of-plane components can be determined by appealing to the zero-traction boundary conditions of the surface under investigation, as in Pantleon (2008); Ruggles and Fullwood (2013); Ruggles et al. (2016). For fully general deformation states, the micrometer-scale Laue x-ray diffraction methods introduced by Larson et al. (2007)) is able to measure the full Nye tensor within the interior of a solid. However the deforming volumes must be of the micrometer length scale and the spatial resolution of the measurements is inferior to that available via EBSD.

Acknowledgments

The authors gratefully acknowledge support from NSF DMR-1310503. In addition, the authors gratefully acknowledge discussions with B. Adams, D. Fullwood, C. F. O. Dahlberg and M. S. Öztop. A. Sarac also gratefully acknowledges the financial support from Ministry of National Education, Turkey.

Supplementary material

Supplementary material associated with this article can be found, in the online version, at 10.1016/j.jmps.2017.11.010.

References

Bassani, J.L., Wu, T.Y., 1991. Latent hardening in single crystal II: analytical characterization and predictions. Proc. R. Soc. Lond. Ser. A 435 (1893), 21–41.
Bastawros, A.F., Kim, K.-S., 2000. Experimental analysis of near-crack-tip plastic flow and deformation characteristics (i): polycrystalline aluminum. J. Mech. Phys. Solids 48 (1), 67–98.
Booker, J.R., Davis, E.H., 1972. A general treatment of plastic anisotropy under conditions of plane strain. J. Mech. Phys. Solids 20, 239–250.
Bruck, H.A., McNeill, S.R., Sutton, M.A., Peters, W.H., 1989. Digital image correlation using Newton–Raphson method of partial differential correction. Exp. Mech. 29 (3), 261–267.
Dahlberg, C.F.O., Saito, Y., Öztop, M.S., Kysar, J.W., 2014. Geometrically necessary dislocation density measurements associated with different angles of indentations. Int. J. Plast. 54, 81–95.
Drugan, W.J., 1986. A more direct and general analysis of moving strong discontinuity surfaces in quasi-statically deforming elastic-plastic solids. J. Appl. Mech. 53 (1), 224–226.
Drugan, W.J., Rice, J.R., 1984. Restrictions on quasi-statically moving surfaces of strong discontinuity in elastic-plastic solids. In: Dvorak, G.J., Shield, R.T. (Eds.), Mechanics of Material Behavior: The Daniel C. Drucker Anniversary Volume. Elsevier Science Publishing Company Inc., New York, pp. 59–73.
Gan, Y.X., Kysar, J.W., 2007. Cylindrical void in a rigid-ideally plastic single crystal III: hexagonal close-packed crystal. Int. J. Plast. 23 (4), 592–619.
Gan, Y.X., Kysar, J.W., Morse, T.L., 2006. Cylindrical void in a rigid-ideally plastic single crystal II: experiments and simulations. Int. J. Plast. 22 (1), 39–72.
Ghazi, N., Kysar, J.W., 2016. Experimental investigation of plastic strain recovery and creep in nanocrystalline copper thin films. Exp. Mech. 56 (8), 1351–1362.
Gurtin, M.E., Anand, L., Lele, S.P., 2007. Gradient single-crystal plasticity with free energy dependent on dislocation densities. J. Mech. Phys. Solids 55 (9), 1853–1878.
Hill, R., 1966. Generalized constitutive relations for incremental deformation of metals crystals by multislip. J. Mech. Phys. Solids 14, 95–102.
Huang, Y., 1991. A user-material subroutine incorporating single crystal plasticity in the ABAQUS finite element program. Technical Report Mech-178. Division of Engineering and Applied Sciences, Harvard University, Cambridge, MA.
Hung, P.-C., Voloshin, A.S., 2003. In-plane strain measurement by digital image correlation. J. Braz. Soc. Mech. Sci. Eng. 25, 215–221.
Kuroda, M., Tvergaard, V., 2008. On the formulations of higher-order strain gradient crystal plasticity models. J. Mech. Phys. Solids 56 (4), 1591–1608.
Kysar, J.W., 1997. Addendum to “A user-material subroutine incorporating single crystal plasticity in the ABAQUS finite element program. Technical Report Mech-178. Division of Engineering and Applied Sciences, Harvard University, Cambridge, MA.
Kysar, J.W., 2000. Directional dependence of fracture in copper/sapphire bicrystal. Acta Mater. 48 (13), 3509–3524.
Kysar, J.W., 2001. Continuum simulations of directional dependence of crack growth along a copper/sapphire bicrystal interface: part I: experiments and crystal plasticity background. J. Mech. Phys. Solids 49 (5), 1099–1128.
Kysar, J.W., 2001. Continuum simulations of directional dependence of crack growth along a copper/sapphire bicrystal interface. Part II: crack tip stress/deformation analysis. J. Mech. Phys. Solids 49 (5), 1129–1153.
Kysar, J.W., Gan, Y.X., Mendez-Arzuza, G., 2005. Cylindrical void in a rigid-ideally plastic single crystal I: anisotropic slip line theory solution for face-centered cubic crystals. Int. J. Plast. 21 (8), 1481–1520.

Kysar, J.W., Saito, Y., Öztop, M.S., Lee, D., Huh, W., 2010. Experimental lower bounds on geometrically necessary dislocation density. Int. J. Plast. 26 (8), 1097–1123.
Larson, B.C., El-Azab, A., Yang, W., Tischler, J.Z., Liu, W., Ice, G.E., 2007. Experimental characterization of the mesoscale dislocation density tensor. Philos. Mag. 87 (8–9), 1327–1347.
Lee, C., Wei, X., Kysar, J.W., Hone, J., 2008. Measurement of the elastic properties and intrinsic strength of monolayer graphene. Science 321 (5887), 385–388.
Lee, D., Wei, X., Chen, X., Zhao, M., Jun, S.C., Hone, J., Herbert, E.G., Oliver, W.C., Kysar, J.W., 2007. Microfabrication and mechanical properties of nanoporous gold at the nanoscale. Scr. Mater. 56 (5), 437–440.
Lee, D., Wei, X., Zhao, M., Chen, X., Jun, S.C., Hone, J., Kysar, J.W., 2007. Plastic deformation in nanoscale gold single crystals and open-celled nanoporous gold. Model. Simul. Mater. Sci. Eng. 15 (1), S181–S192.
Lu, H., Cary, P.D., 2000. Deformation measurements by digital image correlation: implementation of a second-order displacement gradient. Exp. Mech. 40 (4), 393–400.
Nye, J.F., 1953. Some geometrical relations in dislocated crystals. Acta Metall. 1 (2), 153–162.
Öztop, M.S., Kysar, J.W., Niordson, C.F., 2013. Length-scale effect due to periodic variation of geometrically necessary dislocation densities. Int. J. Plast. 41 (1), 189–201.
Pan, B., Qian, K., Xie, H., Asundi, A., 2009. Two-dimensional digital image correlation for in-plane displacement and strain measurement: a review. Measur. Sci. Technol. 20 (6), 062001.
Pantleon, W., 2008. Resolving the geometrically necessary dislocation content by conventional electron backscattering diffraction. Scr. Mater. 58 (11), 994–997.
Peirce, D., Asaro, R., Needleman, A., 1982. An analysis of nonuniform and localized deformation in ductile single crystals. Acta Metall. 30 (6), 1087–1119.
Peirce, D., Asaro, R., Needleman, A., 1983. Material rate dependence and localised deformation in crystalline solids. Acta Metall. 31 (12), 1951–1976.
Rice, J.R., 1973. Plane strain slip line theory for anisotropic rigid-plastic materials. J. Mech. Phys. Solids 21, 63–74.
Rice, J.R., 1987. Tensile crack tip fields in elastic-ideally plastic crystals. Mech. Mater. 6 (4), 317–335.
Ruggles, T.J., Fullwood, D.T., 2013. Estimations of bulk geometrically necessary dislocation density using high resolution EBSD. Ultramicroscopy 133, 8–15.
Ruggles, T.J., Fullwood, D.T., Kysar, J.W., 2016. Resolving geometrically necessary dislocation density onto individual dislocation types using EBSD-based continuum dislocation. Int. J. Plast. 76, 231–243.
Saito, Y., Kysar, J.W., 2011. Wedge indentation into elastic-plastic single crystals, 1: asymptotic fields for nearly-flat wedge. Int. J. Plast. 27 (10), 1640–1657.
Saito, Y., Öztop, M.S., Kysar, J.W., 2012. Wedge indentation into elastic-plastic single crystals. 2: simulations for face-centered cubic crystals. Int. J. Plast. 28 (1), 70–87.
Sarac, A., Öztop, M.S., Dahlberg, C.F.O., Kysar, J.W., 2016. Spatial distribution of the net Burgers vector density in a deformed single crystal. Int. J. Plast. 85, 110–129.
Shield, T.W., Kim, K.-S., 1994. Experimental measurement of the near tip strain field in an iron-silicon single crystal. J. Mech. Phys. Solids 42 (5), 845–873.
Sutton, M.A., Mingqi, C., Peters, W.H., Chao, Y.J., McNeill, S., 1986. Application of an optimized digital correlation method to planar deformation analysis. Image Vis. Comput. 4 (3), 143–150.
Taylor, G.I., 1934. The mechanism of plastic deformation of crystals. Part I. Theoretical. Proc. R. Soc. Lond. Ser. A 145 (855), 362–387.
Uchic, M.D., Dimiduk, D.M., Florando, J.N., Nix, W.D., 2004. Sample dimensions influence strength and crystal plasticity. Science 305 (5686), 986–989.
Vendroux, G., Knauss, W.G., 1998. Submicron deformation field measurements: part 2. Improved digital image correlation. Exp. Mech. 38 (2), 86–92.
Wang, Y., Kysar, J.W., Yao, Y.L., 2008. Analytical solution of anisotropic plastic deformation induced by micro-scale laser shock peening. Mech. Mater. 40 (3), 100–114.
Wei, X., Lee, D., Shim, S., Chen, X., Kysar, J.W., 2007. Plane-strain bulge test for nanocrystalline copper thin films. Scr. Mater. 57 (6), 541–544.
Wu, R., Qian, H., Zhang, D., 2016. Robust full-field measurement considering rotation using digital image correlation. Measur. Sci. Technol. 27 (10), 105002.
Wu, T.Y., Bassani, J.L., Laird, C., 1991. Latent hardening in single crystals i: theory and experiments. Proc. R. Soc. Lond. Ser. A 435 (1893), 1–19.
Yilmaz, M., Kysar, J.W., 2013. Monolithic integration of nanoscale tensile specimens and MEMS structures. Nanotechnology 24 (16), 165502.